remote sensing

Article

Impacts of FY-4A AGRI Radiance Data Assimilation on the Forecast of the Super Typhoon "In-Fa" (2021)

Xuewei Zhang [1], Dongmei Xu [1,2,3,*], Ruixia Liu [4] and Feifei Shen [1,2]

[1] Key Laboratory of Meteorological Disaster, Ministry of Education (KLME)/Joint International Research Laboratory of Climate and Environment Change (ILCEC)/Collaborative Innovation Center on Forecast and Evaluation of Meteorological Disasters (CIC-FEMD), Nanjing University of Information Science & Technology, Nanjing 210044, China
[2] Shanghai Typhoon Institute, China Meteorological Administration, Shanghai 200030, China
[3] The Institute of Atmospheric Environment, China Meteorological Administration, Shenyang 110000, China
[4] The Earth System Modeling and Prediction Centre (CEMC), China Meteorological Administration, Beijing 100081, China
* Correspondence: dmxu@nuist.edu.cn

Abstract: This study assessed the impact of assimilating the Fengyun-4A (FY-4A) Advanced Geosynchronous Radiation Imager (AGRI) observations on the Super Typhoon "In-Fa" event based on the Weather Research and Forecasting Data Assimilation (WRFDA) system of the three-dimensional variational data assimilation (3DVAR) method. It was found that the two water vapor channels 9–10 from the full-disk AGRI datasets yield relatively stable results in terms of the track forecast of In-Fa. A new cloud-detection method using a Particle Filter (PF) was firstly employed to remove the cloud-affected observations by identifying the channel's weighting function. Compared to the other cloud-detection schemes based on the AGRI "Cloud_Binary_Mask" (CLM) products, the PF method is conducive to reducing the track error of typhoon prediction after improving the utilization of observations under clear-sky conditions. Furthermore, the proposed cycling assimilation scheme has a potential positive effect on the intensity forecast of In-Fa. It seems that assimilating the FY-4A AGRI radiance data improves the predictability of Typhoon In-Fa by adjusting the atmospheric environment.

Keywords: data assimilation schemes; cloud detection; Super Typhoon In-Fa; FY-4A AGRI

check for updates

Citation: Zhang, X.; Xu, D.; Liu, R.; Shen, F. Impacts of FY-4A AGRI Radiance Data Assimilation on the Forecast of the Super Typhoon "In-Fa" (2021). *Remote Sens.* **2022**, *14*, 4718. https://doi.org/10.3390/rs14194718

Academic Editors: Dong Liu, Wenbo Sun, Sungsoo Kim, Yongxiang Hu, Gorden Videen and Qiang Fu

Received: 12 August 2022
Accepted: 17 September 2022
Published: 21 September 2022

1. Introduction

In recent years, the improvement in numerical weather prediction (NWP) has been closely related to the development of both advanced satellite detection equipment and the technology of data assimilation systems [1–3]. A considerable number of studies have focused more on polar-orbiting satellite data assimilation, which has been proven to be an effective means of weather forecasting [4–6]. However, some crucial stages in the mesoscale system evolution cannot be continuously monitored by the polar-orbiting satellites. Unlike polar-orbiting satellites, geosynchronous equatorial orbit (GEO) satellites are able to effectively supplement the sparse observations in time and space, which appears especially important for predicting mesoscale weather systems [7].

The assimilation of geostationary satellite radiances has been shown to make a valuable contribution to atmospheric analysis and weather forecasts [8,9]. For instance, the accuracy of precipitation and tropical storm forecasts has been improved with the assimilation of Geostationary Operational Environmental Satellite (GOES)-11/12 and GOES-13/15 radiances, respectively [10,11]. Qin et al. (2018) [12] proved that the Advanced Baseline Imager (ABI) on the GOES-R satellite plays a pivotal role in better estimating both temperature and specific humidity analyses. Following the launch of the new-generation geostationary meteorological satellites, Himawari-8/9, by the Japan Meteorological Agency [13], their series of high-performance instruments have attracted many researchers. An Advanced

Himawari Imager (AHI) experiment with 10 infrared channels generated larger improvements in quantitative precipitation forecasts over the ocean of the southeast coast of China than either an AHI experiment with four GOES-like infrared channels or the control experiments [14]. This was due to additional moisture information in the middle and low troposphere. Similarly, Sawada et al. (2019) [15] showed great progress in the convective predictability of severe rainfall by assimilating the Himawari-8 infrared radiances every 10 min. Advances in the prediction of severe storms could also be traced back to the assimilation of Himawari-8 all-sky infrared radiances [16]. In addition, the impacts of Spinning Enhanced Visible and InfraRed Imager (SEVIRI) on Meteosat Second Generation (MSG) was emphasized by comparison with the polar-orbiting satellite radiances in the Aladin/France numerical weather prediction [17]. The SEVIRI radiances are conducive to the forecast skills of a fast-evolving system based on the different data assimilation schemes [18–20]. Benefits of geostationary satellite radiance assimilation are also of great significance to the prediction of typhoon or hurricane systems. Wang et al. (2017) [21] assimilated the Cross-track Infrared Sounder (CrIS) cloud-cleared radiances from Suomi-NPP for the forecasts of Hurricanes Joaquin (2015) and Matthew (2016). The assimilation of all-sky infrared radiances from Himawari-8 had a positive impact on the two cases of Typhoon Soudelor (2015) and Typhoon Malakas (2016) [22,23]. Simulated radiances of the 183 GHz water vapor absorption band from the future geostationary microwave sounder (GEOMAS) were evaluated for Typhoon Lekima (2019) forecasting in the Weather Research and Forecasting (WRF) model's data assimilation (WRFDA) system [24].

Following the Chinese launch of new-generation geostationary meteorological satellites, the various technical indicators of Fengyun-4A (FY-4A) have achieved the international advanced standard. Considering the demands of atmospheric information, FY-4A was loaded with the advanced technologies of the Advanced Geosynchronous Radiation Imager (AGRI), Geostationary Interferometric Infrared Sounder (GIIRS), Lightning Mapping Imager (LMI), and Space Environment Package (SEP) [25]. Chen et al. (2020) [26] proved the added value of Atmospheric Motion Vectors (AMVs) derived from FY-4A for the analyses and wind forecasts. The capability of monitoring the typhoon core areas by the LMI detector has been confirmed via a comparison with the World Wide Lightning Location Network (WWLLN) [27]. The assimilation of FY-4A GIIRS data was explored by Yin et al. (2021) [28], which demonstrated the efficient performance of higher spectral-temporal resolution radiances in Typhoon Maria (2018) prediction. Furthermore, more research work has been undertaken on the characteristics of FY-4A AGRI datasets. Geng et al. (2020) [29] and Zhu et al. (2020) [30] evaluated the bias characteristics of the AGRI's fourteen channels. They proved that AGRI channels 9–10 have relatively smaller deviations than the AGRI window channels. The atmospheric temperature and humidity could be adjusted by AGRI two water vapor (WV) channels 9–10 [31]. Based on these findings, it is believed that assimilating the high spatial and temporal resolution radiance data of AGRI has the potential to improve the prediction accuracy in NWP models.

The infrared signals affected by clouds are not able to radiate the Earth's surface. Considering the complex cloud-related processes, only infrared radiance data under clear-sky conditions can be assimilated. To be specific, "clear-sky radiance" refers to the part of the observed radiance after discarding a large number of cloud-affected observations. Regarding clear-sky radiance assimilation, cloud detection, as one of the essential procedures, is designed to effectively remove cloud-affected radiance data [32–34]. English et al. (1999) [35] adopted a likelihood method to determine the probability of cloudless conditions given the observations. A channel-dependent cloud-detection algorithm proposed by McNally et al. [36] seeks to identify clear channels by ranking the Infrared channels. For the identification of multi-layer clouds, the Multivariate Minimum Residual (MMR) method minimizes a cost function at each field of view (FOV) [37,38]. A new ensemble-based method for retrieving clouds is proposed in Xu et al. (2016) [39], which applies the Particle Filter (PF) algorithm based on Bayesian theory. The study was the first attempt to apply the new cloud-detection method of PF for infrared radiance assimilation under clear-sky conditions. The unique capability of the proposed PF method is to remove the cloud-affected pixels by identifying the channel's weighting function.

The Super Typhoon In-Fa was one of the most powerful tropical cyclones on record, and caused extensive damages in China. In this study, the impact of FY-4A AGRI satellite data assimilation on the prediction of Typhoon In-Fa was assessed with the three-dimensional variational (3DVAR) method in the WRFDA system. Two cloud-detection schemes were compared for the proposed PF method and the AGRI L2-level products of Cloud_Binary_Mask (CLM). Furtherly, cycling assimilation schemes were designed to enhance the role of AGRI radiance data assimilation in typhoon predictability.

The remainder of this study is structured as follows. A brief introduction to FY-4A AGRI radiances, and the data pre-processing steps, is provided in Section 2. An overview of the typhoon case along with the experimental design is described in Section 3. Section 4 presents the main results, before conclusions and discussions are presented in the last section.

2. Observation, Methodology and Experiments

2.1. AGRI Radiance Data and Pre-process

The FY-4A AGRI enabled great progress to be made in terms of both advanced radiometric accuracy and higher scanning frequency [40]. With 14 spectral bands ranging from visible (VIS) (0.45 µm) to long-wave infrared (IR) (13.8 µm), AGRI is capable of detecting short-term atmospheric circulation changes with respect to the evolution of extreme weather systems. The high spatial resolution of 4000M AGRI L1 Full Disk and 4000M AGRI L1 GEO datasets were considered for data assimilation. The study mainly focused on the AGRI infrared channels 7–14 with the details listed in Table 1. The mid-wave IR channels 7–8 have the capabilities of observing the cloud and surface features. Channels 11–13 are IR window bands with large sensitivities to the topographic conditions. Two IR spectral bands of channels 9–10 and channel 14 are characterized with low atmospheric transmittance and high atmospheric absorbability.

Table 1. Characteristics of FY-4A AGRI for each channel.

Channel	Channel Type	Central Wavelength /µm	Spectral Band /µm	Spatial Resolution /km	Main Application
1	VIS/NIR	0.47	0.45–0.49	1	Aerosol, visibility
2		0.65	0.55–0.75	0.5–1	Fog, clouds
3		0.825	0.75–0.90	1	Aerosol, vegetation
4	Shortwave IR	1.375	1.36–1.39	2	Cirrus
5		1.61	1.58–1.64	2	Cloud, snow
6		2.25	2.10–2.35	2–4	Cloud phase, aerosol, vegetation
7	Midwave IR	3.75	3.50–4.00	2	Clouds, fire, moisture, snow
8		3.75	3.50–4.00	4	Land surface
9	Water vapor	6.25	5.8–6.7	4	Upper-level WV
10		7.1	6.9–7.3	4	Midlevel WV
11	Longwave IR	8.5	8.0–9.0	4	Volcanic ash, cloud-top phase
12		10.7	10.3–11.3	4	SST, LST
13		12.0	11.5–12.5	4	Clouds, low-level WV
14		13.5	13.2–13.8	4	Clouds, air temperature

Figure 1 shows the averaged weighting functions of the AGRI channels 8–14 calculated by the Radiative Transfer for TIROS Operational Vertical Sounder (RTTOV) model based on the atmospheric profiles of the background. For clear-sky radiance assimilation, the cloud inputs are set to zero in the RTTOV calculation. The 12 h spin-up forecast is provided as the background based on the NCEP operational 0.25° × 0.25° GFS analysis datasets as inputs to the RTTOV. Generally, channel 9 (5.8–6.7 m) and channel 10 (6.9–7.3 m) have peaks of the weighting function around 250 and 400 hPa, respectively, representing the water vapor information in the upper and middle troposphere. The carbon dioxide absorption of channel 14 peaks at roughly 600 hPa, detecting the low-level temperature. In this study, the weighting functions calculated by the background atmosphere are reasonable, although slightly different from the U.S. standard atmosphere results [26].

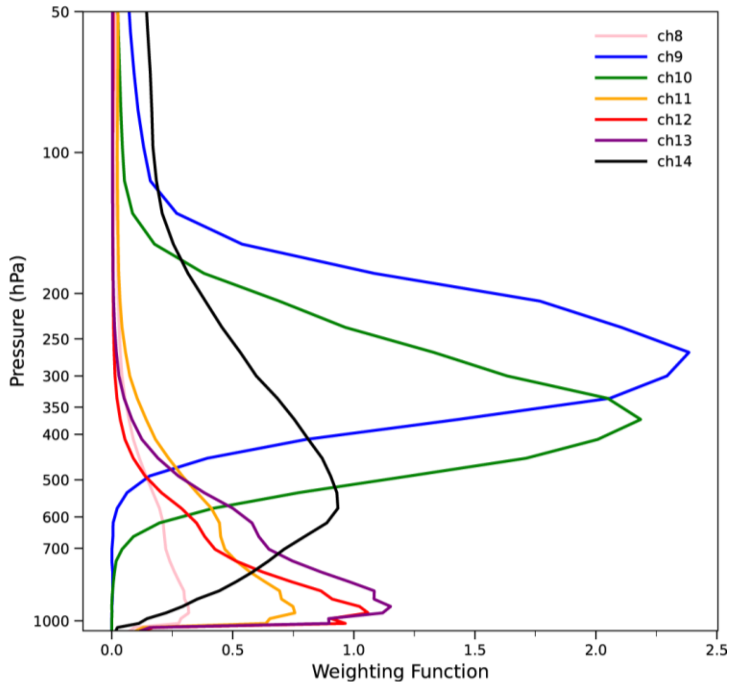

Figure 1. The distributions of weighting function of AGRI infrared channels 8–14 calculated using the background atmospheric profiles as the input for the RTTOV radiative transfer model.

2.1.1. Quality Control and Bias Correction

Prior to the data assimilation, the QC procedure is conducted. The reasonable process of QC is able to remove large differences between the expected values and the observations (Geer et al., 2011) [41]. In this study, the AGRI observations were pre-processed, including the following steps:

(1) Rejecting all channels with mixed surface types of observation data.
(2) Rejecting the observations of channel 8 and channels 11–13 that are greatly affected by uncertain surface parameters [30].
(3) Rejecting the observation pixels where satellite zenith angels are larger than 60°.
(4) Rejecting the observations if the absolute innovation (bias-corrected observation minus simulated background) exceeds 3 times the observation error under clear-sky conditions, and if it exceeds 15 K.
(5) Rejecting cloudy pixels with the PF cloud-detection method, which is described in Section 2.3.

The quality of radiance assimilation is also degraded by the inter-correlation between channels and by systematic bias. Thereby, additional steps for spatial thinning and variational bias correction (VarBC) were carried out before the assimilation. A thinning mesh of 45 km for all the experiments was used to lessen the potential error correlations among adjacent observations [42]. The applied predictors for VarBC are the constant 1000–300 hPa and 200–50 hPa layer thicknesses, surface skin temperature, and total column precipitable vapor, without considering the satellite zenith angle [29]. The correction coefficients were firstly achieved from offline statistics, which were then updated frequently with each analysis.

2.1.2. Cloud Detection

The fast radiation transfer model of RTTOV was designed to calculate the radiance as an observation operator under clear-sky or all-sky conditions [43]. While in a complex environment having clouds, scattering and refraction of aerosol particles are severely intensified, causing a large FG departure (the observation minus the first guess) from the Gaussian distribution. Thus, cloud detection is crucial as a part of the QC procedures to assimilate clear-sky radiances. The PF cloud-detection technique is incorporated here into the WRFDA system.

In this study, $C = c^0, c^1, c^2, \ldots, c^K$ is used to denote the array of vertical effective cloud fractions for K model levels (c^1 for the surface and c^K for the model top) and c^0 is the fraction of clear sky. The constraint for the cloud fraction is as follows:

$$\sum_{k=0}^{K} c^k = 1,\ 0 \le c^k \ \le 1,\ \forall k \in [0, K]. \tag{1}$$

The construction of the cloud fractions is based on the idea that the radiative effect of the cloud is modeled by a stack of thin black clouds for K vertical model levels. At each level k, the cloud fraction c^k seen by the satellite is assumed to be independent of frequency v. Every fractional cloud at level k completely blocks the radiation at lower levels. In this case, the concept of cloud overlap can be ignored. The radiation originating from the lower levels is assumed to contribute to the top of atmosphere radiance transmitted to the satellites only with the residual fractions. Thus, the simulated radiance R_v^{cloud} with the different frequencies v in full-weather conditions is defined as:

$$R_v^{cloud}\left(c^0, c^1, c^2, \cdots, c^K\right) = c^0 R_v^0 + \sum_{k=1}^{K} c^k R_v^k\,, \tag{2}$$

where R_v^k means the calculated radiance assuming an overcast black cloud at the model level k and R_v^0 denotes the radiance calculated in the clear sky. Both R_v^k and R_v^0 are calculated using a forward radiative transfer model with model profiles of temperature and moisture as inputs. The cloud profiles are firstly initialized as particles and the retrieved cloud profile is obtained by averaging those particles with their weights, as follows:

$$\omega^i = e^{-\sum_v \left(\frac{R_v^{obs} - R_{v,i}^{cloud}}{\sigma_v}\right)^2} \tag{3}$$

Each particle's weight ω^i is computed as Equation (3) through the specified observation error of σ_v, the difference-value between the simulated cloudy radiance from the particle $R_{v,i}^{cloud}$, and the observed radiance R_v^{obs}. The final retrieved cloud fraction C_a is determined based on the weight averaged particles of the cloud fraction using $C_a = \sum_{i=1}^{p} \omega^i C^i$. Here, p is the total number of particles and C^{i} is the i^{th} particle. The cloud-detection process was undertaken for every pixel in the AGRI scene. A detailed description of the PF method can be found in Xu et al. (2016) [39].

Furthermore, some channels are determined to be cloud-contaminated when the difference between the calculated radiance R_v^0 under the clear-sky and the simulated cloudy radiance R_v^{cloud} based on the determined cloud fraction profile C_a is larger than a predetermined threshold 0.01, as:

$$\frac{\left|R_v^0 - R_v^{cloud}\right|}{R_v^0} > 0.01\,. \tag{4}$$

In addition, another cloud-detection scheme was designed based on the FY-4A AGRI CLM products. The high quality of AGRI CLM datasets was confirmed in the research of

Wang et al. (2019) [44], by comparing with them with cloud products from Himawari-8 and MODIS. The value for the CLM is identified as 0 for cloud, 1 for probably cloud, 2 for probably clear, and 3 for clear on one pixel. In this study, data assimilation experiments based on the CLM products were provided as a benchmark against those based on the PF scheme.

2.2. The Data Assimilation System

The WRFDA system was developed by the National Center for Atmospheric Research (NCAR), and consists of 3DVAR, four-dimensional variational DA (4DVAR), and Hybrid DA techniques. The new version 4.3 of WRF-3DVAR (WRF three-dimensional variational data assimilation) system was applied to obtain an optimal variance estimate of the real atmospheric state called "the analysis field" by iteratively minimizing the cost function as follows [45]:

$$J(\boldsymbol{x}) = J_b + J_o = \frac{1}{2}(\boldsymbol{x} - \boldsymbol{x}_b)^{\mathrm{T}}\mathbf{B}^{-1}(\boldsymbol{x} - \boldsymbol{x}_b) + \frac{1}{2}[\boldsymbol{H}(\boldsymbol{x}) - \boldsymbol{y}_o]^{\mathrm{T}}\mathbf{O}^{-1}[\boldsymbol{H}(\boldsymbol{x}) - \boldsymbol{y}_o] \quad (5)$$

where $\boldsymbol{x}_b$ is the background state vector with the background error covariance matrices $\mathbf{B}$, and $\boldsymbol{y}_o$ is the observation vector with the observation error covariance matrix $\mathbf{O}$. The background error statistics were computed using the National Meteorological Center (NMC) method based on the NCEP background error covariance of CV5 [46]. In this study, the RTTOV was used as the nonlinear observation operator $\boldsymbol{H}(x)$, which converts the model variables into the simulated radiance for the AGRI radiance assimilation.

2.3. Overview of Typhoon In-Fa

According to the China Meteorological Administration (CMA) record (Figure 2), a tropical depression formed at 1800 UTC 17 July 2021 over the Pacific Northwest Ocean. By the extraction of heat energy from the powerful Kuroshio warm current, it rapidly developed as Super Typhoon In-Fa with a maximum wind speed (MWS) of 45 m/s and a minimum sea level pressure (MSLP) of 955 hPa at 0300 UTC 21 July. After 0600 UTC 23 July, In-Fa abruptly twisted from the north-west to the north-north-west due to the weak steering flow and the joint Typhoon Cempaka. When closer to the south-west side of the subtropical high, In-Fa propagated north-westward and then entered Zhejiang Province around at 0430 UTC 25 July. The warm moist flow carried by In-Fa was continuously delivered from the ocean to the central and eastern coastal areas of China, leading to serious rainstorm disasters. However, it was difficult to make an accurate forecast of the Typhoon In-Fa due to the higher intensity and anomalously slow speed of the movement.

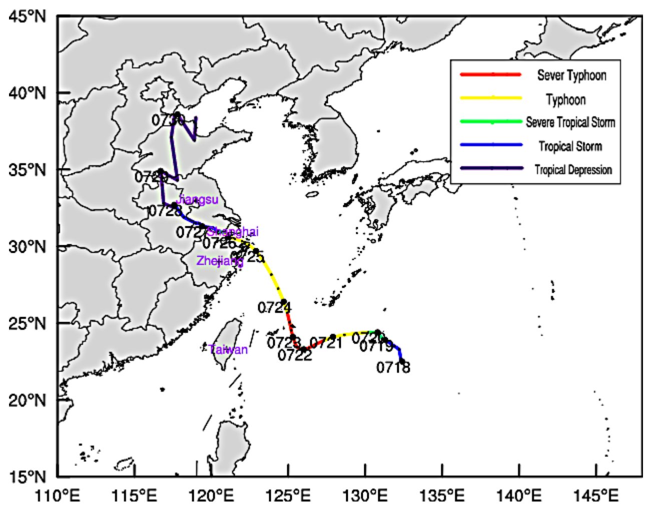

Figure 2. The best-track and intensity evolution for Super Typhoon In-Fa every 24 h from 18 July 2021 to 30 July 2021.

2.4. Experiment Setup

All the experiments employed version 4.3 of the WRF model. For the forecasts of Typhoon In-Fa, the model domain covers the western Pacific Ocean and the southeast coast of China, having a 9 km grid spacing on 721 $\times$ 541 horizontal grids and 43 vertical levels up to 50 hPa. The parameter setting of physical schemes was set as following: the WRF Single-Moment 6-Class scheme [47]; the RRTMG shortwave and longwave schemes [48]; the Yonsei University (YSU) boundary layer scheme [49]; the Revised MM5 scheme for near-surface layer process [50]; and the Unified Noah land surface model for land surface [51]. The experiments differed in several aspects, as detailed in Table 2.

Firstly, the sensitivity experiments on channel selection here only account for the performance of AGRI channels 9–10 and channel 14 by adding the Cyc, Cyc_Ch9/10/14, and Cyc_Ch10 experiments. To assess the ability of the new PF method, the experiment Cyc with the PF method was compared with the experiments of Cyc_CLM0 and Cyc_CLM2 based on the AGRI CLM products for the cloud detection. The Cyc_CLM0 experiment only rejected the data flagged as being cloudy, with more observations being assimilated. The experiment of Cyc_CLM2 rejected all the data flagged as cloudy, probably cloudy, and probably clear.

In addition, the cycling experiment of Cyc was further designed to assimilate the full-disk FY-4A AGRI data using inter-3 h data assimilation cycling (DA cycling) schemes, while the experiments of SingleDA_06 and SingleDA_12 without DA cycling only conducted one-time data assimilation. To be specific, in the experiments of SingleDA_06 and SingleDA_12, the data assimilation was only valid at 0600 UTC 23 July and 1200 UTC 23 July, respectively. Deterministic forecasts at 48 and 42 h were further launched for SingleDA_06 and SingleDA_12. Note that the first assimilation cycle started at 0600 UTC 23 July in all the experiments, except for the SingleDA_12 experiment, which initialized its first assimilation at 1200 UTC 23 July. The flowchart of all the experiments is illustrated in Figure 3.

Table 2. The setting of all the assimilation experiments.

Experiment	Cloud-Detection Scheme	DA Cycling Scheme	Channel Selection	Purpose of Experiments
SingleDA_06	PF	No DA cycling, valid at 0600 UTC	Channel 9/10	Sensitivity of data assimilation design strategies
SingleDA_12		No DA cycling, valid at 1200 UTC		
Cyc_CLM0	CLM_0: reject cloudy pixels	Inter-3 h DA cycling, valid at 0600, 0900, 1200 UTC		Sensitivity of cloud-detection schemes
Cyc_CLM2	CLM_2: reject cloudy pixels, probably cloudy, and probably clear pixels			
Cyc	PF			Benchmark for sensitivity experiments
Cyc_Ch9/10/14			Channel 9/10/14	Sensitivity of channel selection
Cyc_Ch10			Channel 10	

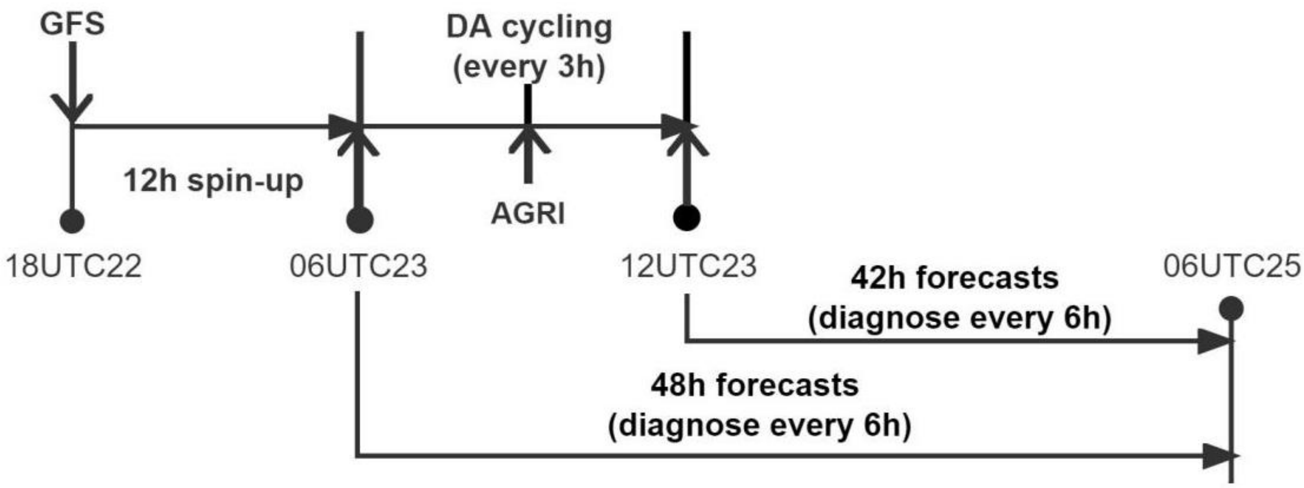

Figure 3. The flow charts of all the experiments listed in Table 2.

3. Results and Discussion

In this section, evaluations of initialization and subsequent forecasts for Typhoon In-Fa are conducted based on the sensitivity experiments of the channel selection, cloud detection, and design strategies of data assimilation. Diagnostics are shown to reveal how the difference in the analysis contributed to the difference in the forecasts. The best track, MWS, and MSLP for Typhoon In-Fa are from the CMA records.

3.1. Channel Sensitivity

The sensitivity experiments on channel selection were conducted in terms of two water vapor channels (channels 9 and 10) and one carbon-dioxide-sensitive channel (channel 14) for Typhoon In-Fa prediction. In Figure 4a,b, it is found that the capability of the Cyc experiment with the AGRI channels 9–10 is the best in terms of the track prediction. To be specific, the mean track error in the Cyc experiment was roughly 8 km lower than that in the Cyc_Ch9/10/14 experiment and 10 km less than that of the Cyc_Ch10 experiment. The assimilation of channels 9–10 and channel 14 in the Cyc_Ch9/10/14 experiment shows an overall smaller error in the typhoon track compared to the Cyc_Ch10 experiment with the single channel 10, as shown in Figure 4b. The mean range error of the Cyc_Ch10 experiment increased clearly after 24 h, up to roughly 127.9 km. In terms of the typhoon intensity, all the experiments tend to show lower MSLP and MWS versus the best track (Figure 4c,d). It is noted that the MLSP and MWS prediction are comparable across different channels, which is likely due to the fact that the ability to depict the inner-core structures of In-Fa is limited with the clear-sky AGRI radiance data assimilation. On the whole, it seems that the additional channel 14 did not contribute to the improvements in the typhoon track or intensity forecasts.

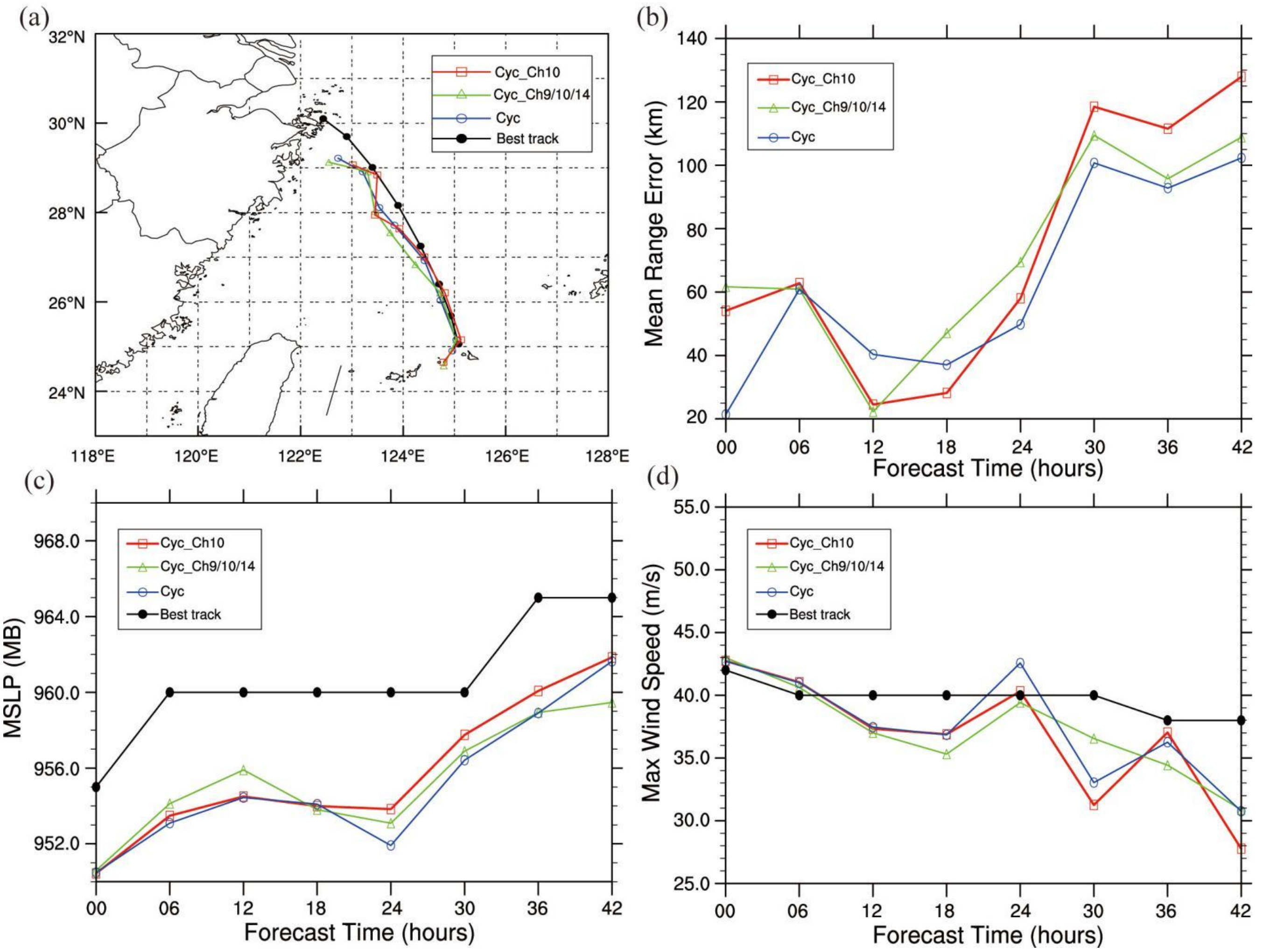

Figure 4. The predicted (**a**) tracks, (**b**) track errors, (**c**) minimum surface level pressure (hPa), and (**d**) max wind speed (m/s) in the Cyc (blue lines), Cyc_Ch9/10/14 (green lines), and Cyc_Ch10 (red lines) experiments are compared to the CMA best-track estimates (black lines) from 1200 UTC 23 July 2021 to 0600 UTC 25 July 2021.

3.2. Cloud Detection

Figure 5 shows the observed cloudiness denoted by the brightness temperature of wind channel 12 and the distributions of the brightness temperature in the Cyc, Cyc_CLM0, and Cyc_CLM2 experiments with different cloud-detection schemes for AGRI channels 9 and 10 respectively. The counts of observations for both channel 9 and channel 10 are the same as without QC; for example, the count is marked on the top right in Figure 5b as 10,841. As shown in Figure 5a,c, the rejected radiances after QC are generally distributed out of the typhoon vortex. The brightness temperature distributions from the channel 9 observations (without QC) are consistent with the observed cloudiness.

Figure 5c,d show the pixels after the cloud detection in Cyc experiments with the same PF method for AGRI channels 9 and 10, respectively. It is noticeable that the brightness temperature of channel 9 is colder than that of channel 10 due to its higher weighting function peak. Furthermore, the retained observation data for the higher levels of channel 9 are greater than those for the lower levels of channel 10. It is expected that the improved utilization of AGRI radiance data may be favorable for the initial conditions in typhoon forecasts.

Figure 5e,f show the cloud-detection results for the same channel 10 but in the different experiments of Cyc_CLM0 and Cyc_CLM2. Cyc_CLM0 retains clear, probably clear, and probably cloudy data, while Cyc_CLM2 only utilizes clear data. It can be found that the rough distribution of cloud pixels observed by Cyc with the PF method (Figure 5d) has a good spatial correspondence with the other experiments using CLM products (Figure 5e,f). As expected, some observations in the cloudless area can be effectively retained through the PF method, while these observations are mistakenly classified as "cloudy", and thus rejected in the experiments with CLM products. From Figure 5, it is possible to conclude that the PF cloud-detection scheme is capable of efficiently detecting radiances that are free of clouds.

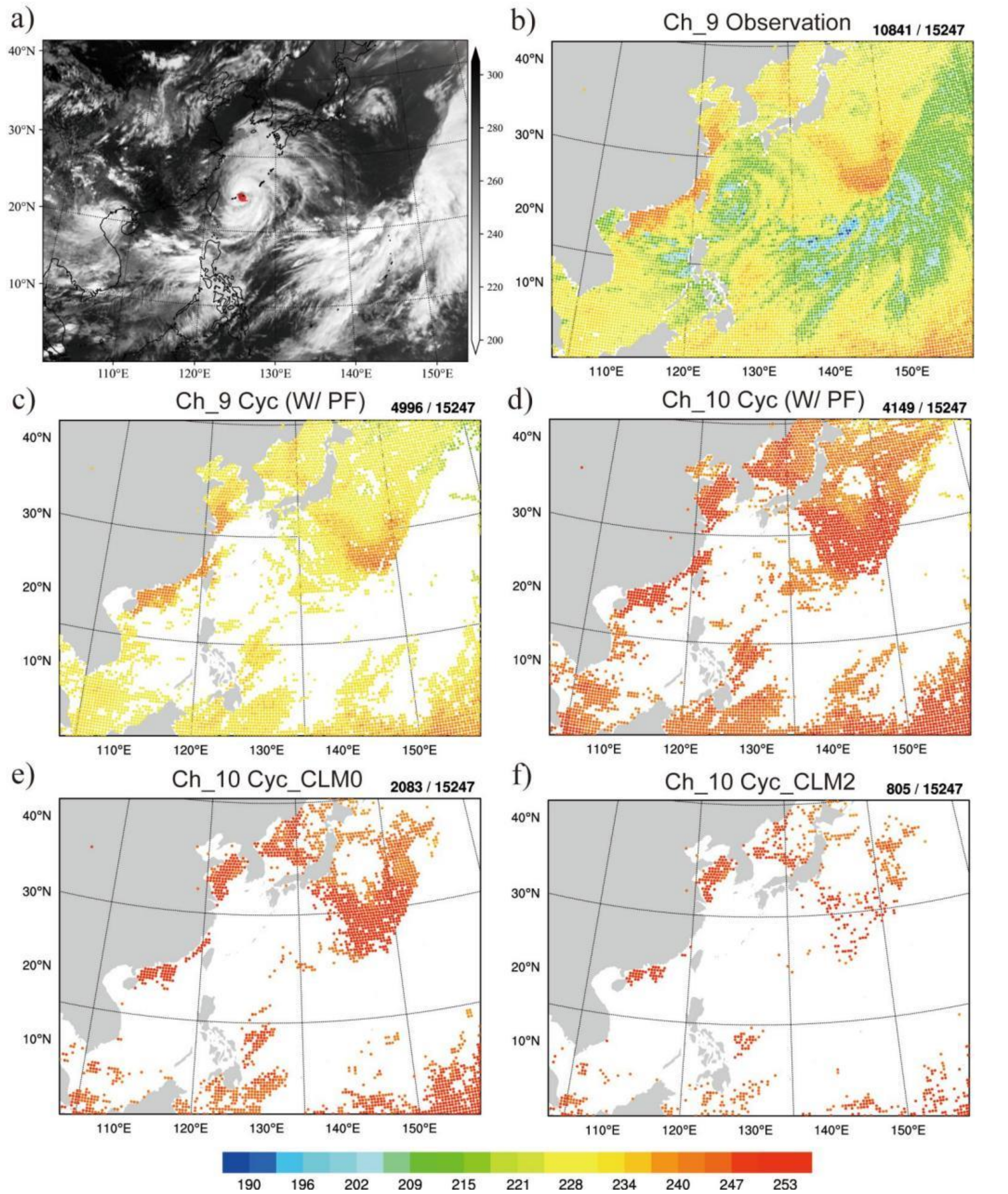

Figure 5. (**a**) The brightness temperature of the AGRI window band 12 (with central wavelength of 10.8 μm) with the location of Typhoon In-Fa (denoted by a red mark). The observed brightness temperature (unit: K) distributions from (**b**) the observation without QC for channel 9, (**c**) the Cyc experiment with the PF method for channel 9, (**d**) the Cyc experiment with the PF method for channel 10, (**e**) the Cyc_CLM0 experiment for channel 10, and (**f**) the Cyc_CLM2 experiment for channel 10 valid at 0600 UTC 23 July 2021. The numbers on the top right represent the used-data counts versus the total-data counts in each assimilation experiment.

Figure 6 illustrates the used-data counts in the experiments of Cyc, Cyc_CLM0, and Cyc_CLM2 with different cloud-detection schemes valid at the first and the last analysis cycle. It can be seen that the counts of observations in the Cyc experiment with the PF method are obviously higher compared to the other experiments with the CLM schemes after the cloud detection, which is consistent with the results illustrated in Figure 5. In addition, the significant differences in data counts between channels 9 and 10 range from 847 to 1077 in the Cyc experiments, whereas the counts of channels 9 and 10 are comparable overall in the CLM-based experiments. This suggests that more observations could be assimilated for channel 9, having higher peaks of the weighting function, than for channel 10, having lower peaks, due to the unique abilities of the PF method. Overall, the counts of used data in all the experiments increased with the analysis-forecast cycles after the model spin-up.

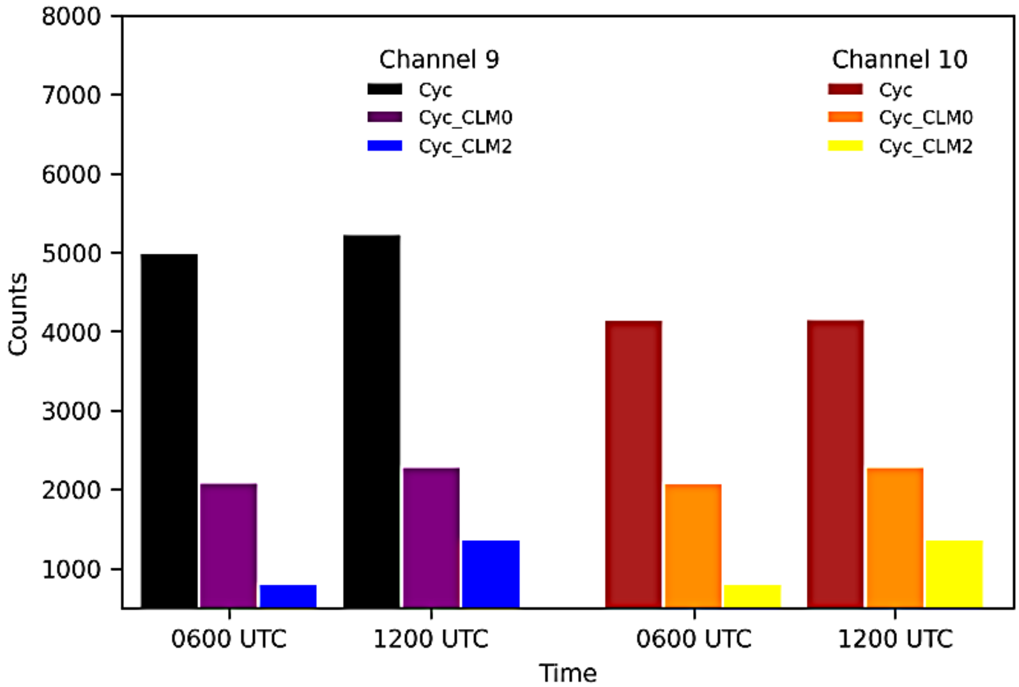

Figure 6. The counts of observations for AGRI channels 9–10 from the Cyc, Cyc_CLM0, and Cyc_CLM2 experiments, valid at 0600 UTC 23 July 2021 and 1200 UTC 23 July 2021.

Figure 7 shows the 42 h track forecasting results in the experiments with different cloud-detection schemes from 1200 UTC 23 July 2021 to 0600 UTC 25 July 2021. It can be seen that the Cyc experiment with the PF method yields the typhoon track prediction with enhanced accuracy after 18 h forecasts versus the other experiments based on the CLM schemes (Figure 7b). By comparison, the typhoon movement speed in the Cyc experiment is relatively faster and closer to the best track (Figure 7a). The results imply that the period validity in the PF-based experiments is more durable and stable for the typhoon track forecasting.

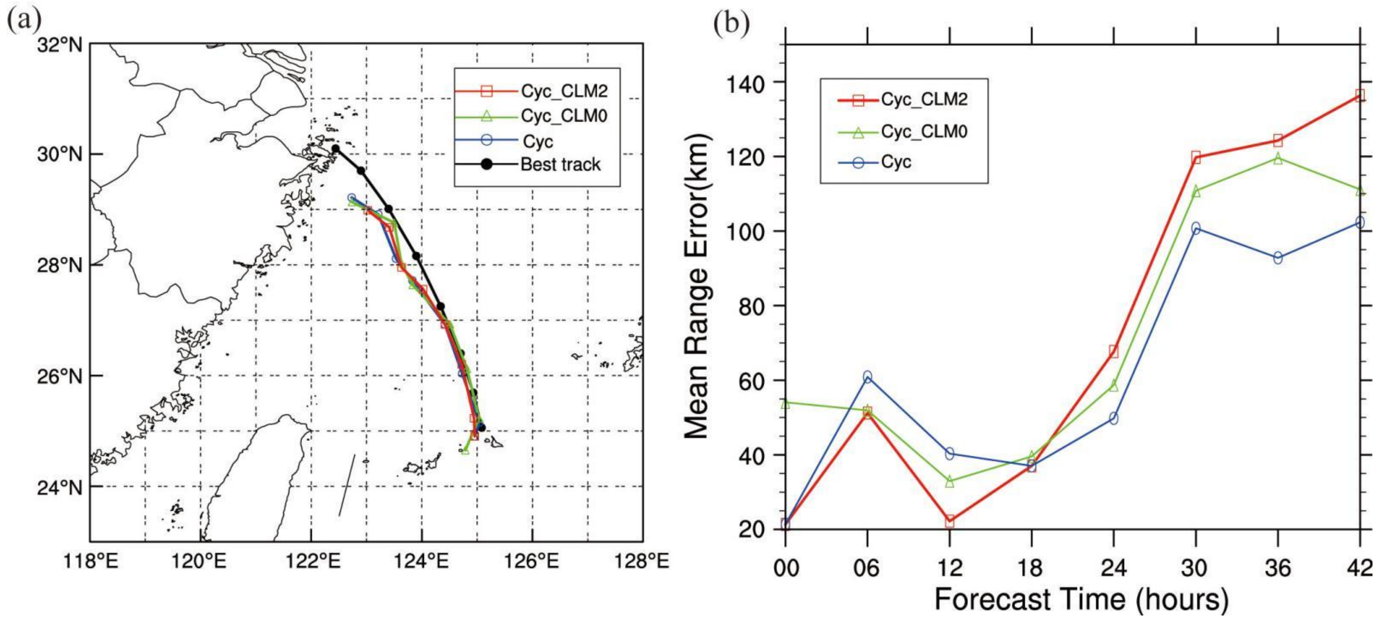

Figure 7. The 42 h predicted (**a**) tracks and (**b**) mean track errors (units: km) in the different experiments of Cyc (blue lines), Cyc_CLM0 (green lines), and Cyc_CLM2 (red lines) are compared to the CMA best-track data (black lines) from 1200 UTC 23 July 2021 to 0600 UTC 25 July 2021.

3.3. Data Assimilation Design Strategies

In this section, the three experiments Cyc, SingleDA_06, and SingleDA_12, having different design strategies of data assimilation, are further assessed based on the PF method using the radiances of FY-4A AGRI channels 9–10. The sensitivity experiments included the comparison of single and multiple DA cycling schemes, and different initial times for the data assimilation.

3.3.1. Impact on the Analysis

The impacts of different assimilation schemes are evaluated by analyzing the 500 hPa geopotential height related to the typhoon track evolution. The forecasts are compared with the ERA-Interim reanalysis from the European Centre for Medium-Range Weather Forecast (ECMWF) as the reference [52]. The main factors affecting Typhoon In-Fa's track are the subtropical high and the continental high, located on the north-west and north-east sides of In-Fa, respectively (Figure 8). In Figure 8a,d, it seems that the SingleDA_06 experiment valid at 0600 UTC 23 July describes a stronger subtropical high and the continental high pressure was located further north, which is more consistent with the ERA-Interim reanalysis indicated by the red arrows. The SingleDA_06 experiment may have the potential to produce improved typhoon tracks. Regarding the SingleDA_12 experiment valid at 1200 UTC 23 July, the strong continental high pressure is located to the south (Figure 8c), thereby squeezing the Typhoon In-Fa moving north-eastward. In the Cyc experiment with the DA cycling scheme, the subtropical high center of the maximum pressure is closer to the powerful low-pressure system In-Fa and the wind speed is high, as marked with a black rectangle in Figure 8b. Thus, the pressure gradient between these two systems tends to be sharp, resulting in the accelerated typhoon track speed.

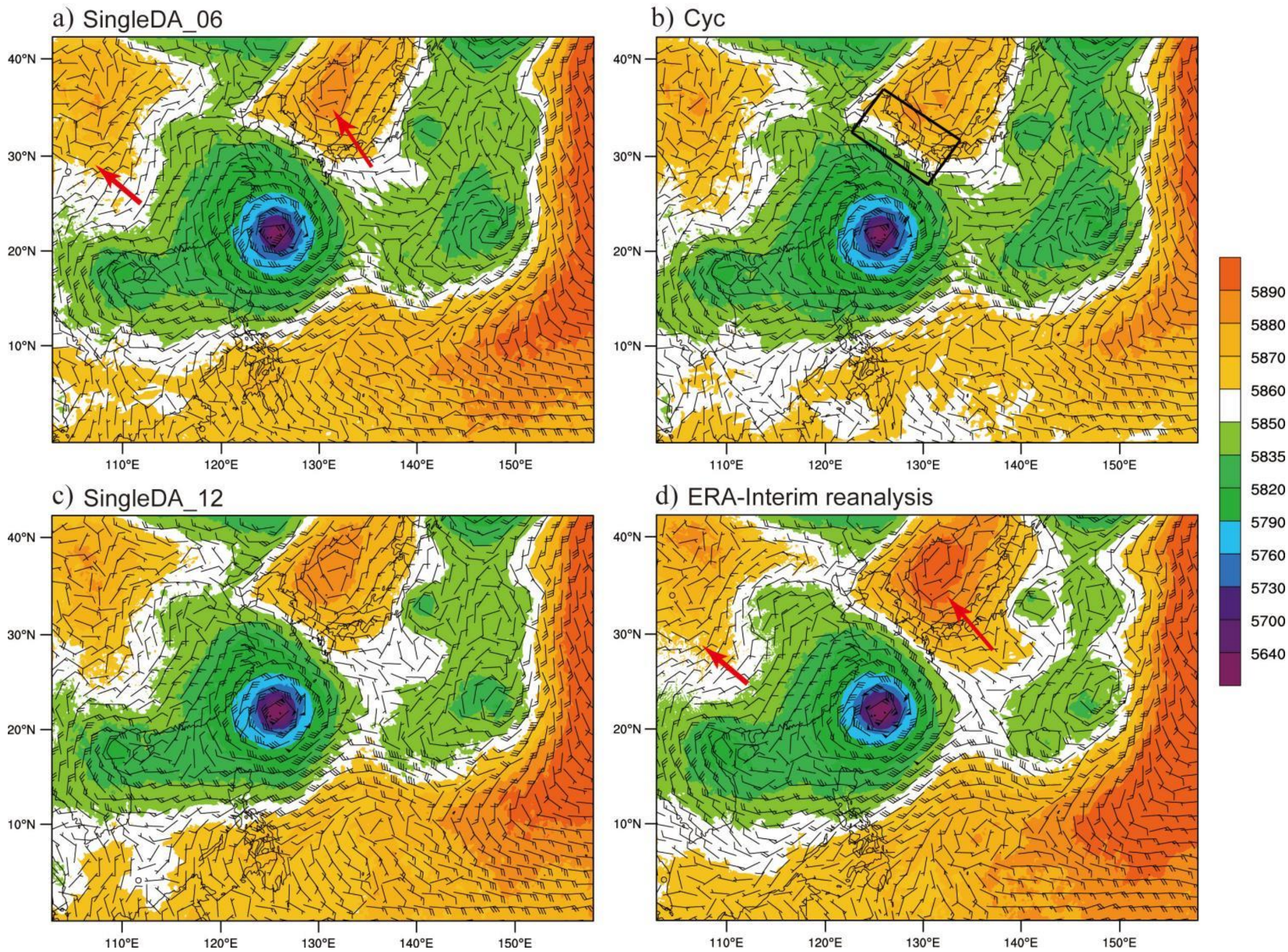

Figure 8. The 500 hPa geopotential height (shaded, units: gpm) and wind field (wind shaft, units: m/s) from the (**a**) SingleDA_06, (**b**) Cyc, (**c**) SingleDA_12 experiments, and (**d**) corresponding ERA-Interim reanalysis fields valid at 1200 UTC 23 July 2021.

The evolution of the geopotential height analysis increments (the analysis from the data assimilation minus the background for the data assimilation that is the 12 h spin-up forecast) at 500 hPa are illustrated at different assimilation cycles from the Cyc experiment. The typhoon positions from CMA (black dot) are plotted in Figure 9. After each verifying time, the positive increments are amplified over most of the domain as marked with the numbers, especially near the typhoon center, which can weaken the strength of Typhoon In-Fa. In the Cyc experiment with DA cycling schemes, In-Fa has decreased in strength, which is consistent with a significant improvement in the MSLP, as shown in Figure 10c. In Figure 9c, valid at the last cycle analysis, a notable dipole structure is observed with an increase and a decrease in the north-east and south-west of the typhoon center, respectively. It can also be noticed that the Cyc experiment generates a large area of high geopotential height extending from Korea to Japan near the location of the subtropical high. The atmospheric circulation after DA cycling tends to move In-Fa south-westward, as shown by the forecast tracks in Figure 10a.

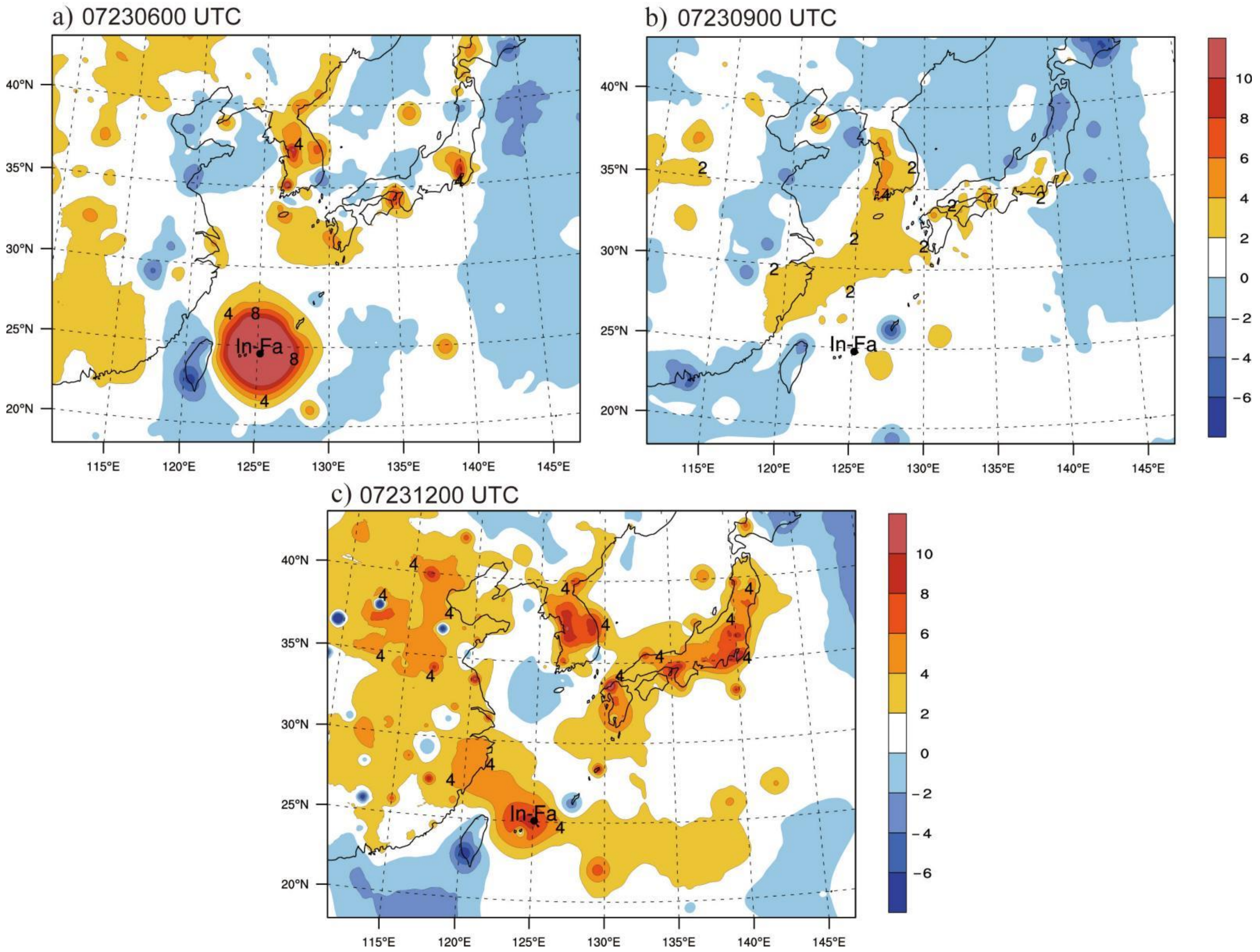

Figure 9. The 500 hPa geopotential height increments (the analysis from the data assimilation minus the background for the data assimilation that is the 12 h spin-up forecast) (shading, units: gpm) in the Cyc experiment valid at (**a**) 0600 UTC 23 July 2021, (**b**) 0900 UTC 23 July 2021, and (**c**) 1200 UTC 23 July 2021. The typhoon center is denoted as the black dot. The numbers show the positive increments of geopotential height.

3.3.2. Impacts on the Typhoon Forecasts

After evaluating the impacts of assimilation schemes on the analysis, the consequent forecasts of Typhoon In-Fa are exhibited in Figure 10 during the same period from 1200 UTC 23 July to 0600 UTC 25 July 2021, when the intensity level of In-Fa changes. Figure 10a shows that the SingleDA_06 experiment started at 0600 UTC 23 July matches best with the best track, while the SingleDA_12 experiment with a different initial time and the control experiment (Ctrl) without data assimilation both yield a north-east track bias after 18 h. In the first 12 h, the mean absolute track error from Ctrl is lower than that of the other experiments (Figure 10b). It is noted that the AGRI data assimilation experiments do not outperform the control experiment, especially at the beginning of the forecast, which is likely caused by the incompatible thermodynamic field after the data assimilation. This imbalance will be alleviated after the integration of the NWP models. Although there is an increasing south-westward bias in the Cyc experiment after 24 h, a slight improvement in the movement speed forecast was achieved based on the DA cycling scheme. The average track error in Cyc appears to be effectively reduced after 12 h.

The 42 h evolutions of the typhoon intensity for the MSLP and MSW are shown in Figure 10c,d. According to the results, the MSLP in all the experiments is generally stronger than the best track and the forecast tracks lag behind the observed track. It is shown that the MSLP in the Cyc experiment with the DA cycling scheme is the most consistent with the best-track data. The limited intensity improvement from other experiments may have been constrained by the lack of a DA cycling procedure with the AGRI radiances. In terms of MWS, deterministic forecasts from the data assimilation experiments are in better agreement with the best records than the Ctrl experiment. From Figure 10c,d, the largest intensity errors are observed in the Ctrl experiment, reaching 22.4 hPa in MSLP and 8.3 m/s in MWP forecasts. It seems that assimilating the AGRI radiances, especially with the cycling schemes, more directly adjusted the pressure field and wind field, leading to a more rapid impact on the typhoon intensity.

It is also interesting to note that the analysis initialized at 0600 UTC 23 July yields better track and intensity forecasts than the analysis initialized at 1200 UTC 23 July. This may be because a more balanced typhoon environment is created at the earlier stage of Typhoon In-Fa than that at a later period. Different initial times of data assimilation may lead to the diverse forecast accuracy.

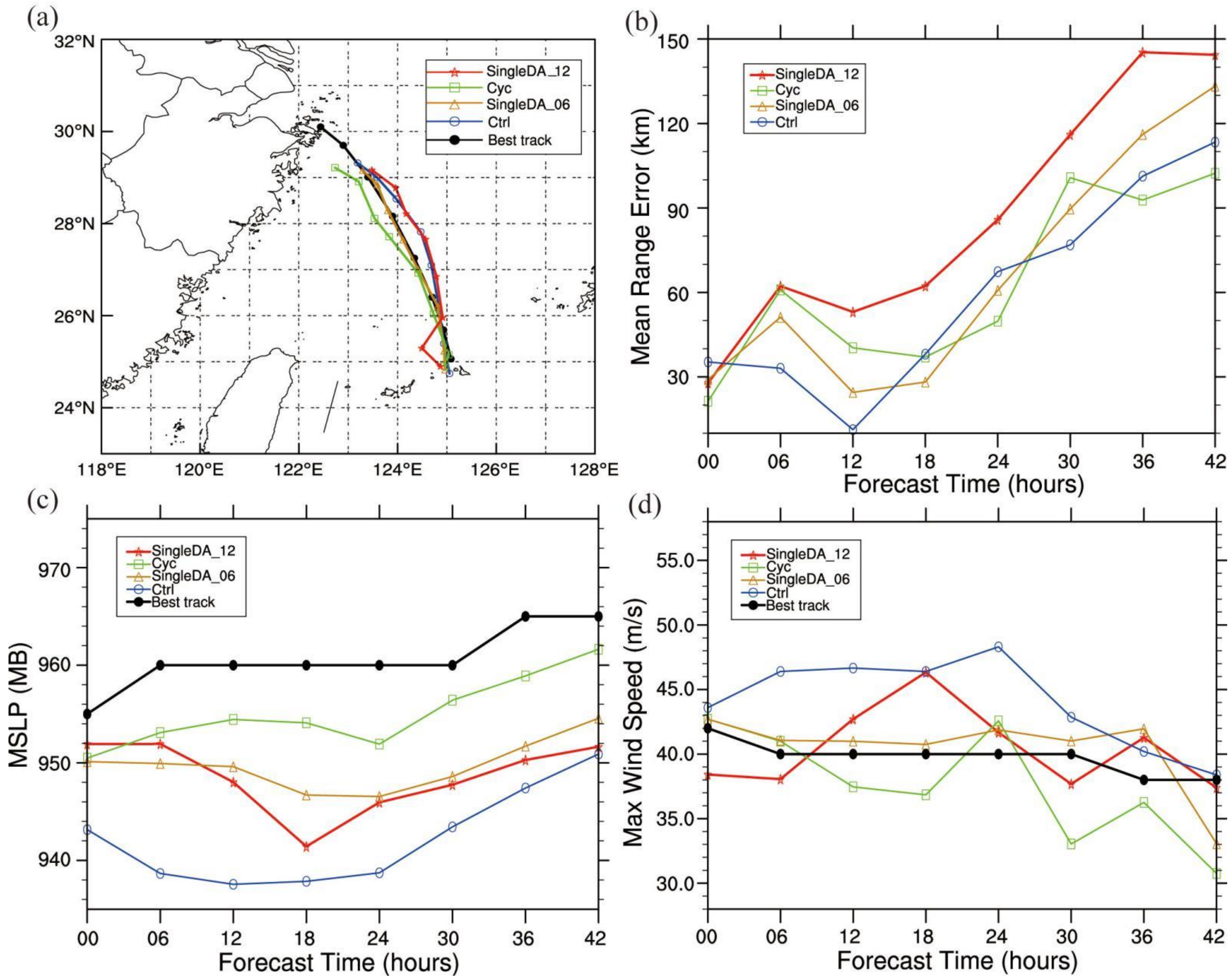

Figure 10. The 42 h predicted (**a**) tracks, (**b**) track errors, (**c**) minimum surface level pressure (hPa), and (**d**) maximum surface wind speed (m/s) of Typhoon In-Fa in the SingleDA_06 (orange lines), SingleDA_12 (red lines), Cyc (green lines), and control (blue lines) experiments, compared to the CMA best data (black lines) from 1200 UTC 23 July 2021 to 0600 UTC 25 July 2021.

4. Summary and Future Perspective

The impact of assimilating the FY-4A AGRI radiances was assessed with the WRF-3DVAR system for the analysis and forecasts of Super Typhoon In-fa. The AGRI satellite data processing was conducted in three types of sensitivity experiments, namely, the channel selection, cloud detection, and data assimilation design strategies. It was found that the two water vapor channels 9–10 from the full-disk AGRI data yield relatively stable results in terms of the track forecast for In-Fa according to the channel sensitivity experiments. Due to the capability of identifying the channel's weighting function, more observations could be efficiently assimilated in the experiments with the PF method compared to those based on the AGRI CLM products for cloud detection. Furthermore, the experiments with the PF method yield a reduction in the error of the typhoon track forecasts. Other data assimilation design strategies were further investigated, including cycling assimilation schemes and different assimilation times, by comparing the forecast results of Typhoon In-Fa. The proposed DA cycling schemes were demonstrated to be an efficient approach to improve the intensity forecast of Typhoon In-Fa. Based on the rational scheme, the assimilation of the FY-4A AGRI satellite data has a relatively positive impact on the forecast of Typhoon In-Fa by adjusting the atmospheric environment.

The above conclusions can be instructive in assimilating the FY-4A AGRI observations for prediction of super typhoons. Future studies are needed with more typhoon cases over extended periods. Despite the above encouraging results, forecast biases in terms of typhoon movement speed were observed. Future work will likely address using more advanced data assimilation, such as four-dimensional variation assimilation (Xiao et al., 2020), hybrid-variation assimilation (Sun et al., 2021), or all-sky assimilation, to better utilize FY-4A AGRI data in a flow-dependent manner at appropriate times (Xu et al., 2021). The refinement of the bias correction and observation errors will also be explored to further improve the performance of FY-4A AGRI radiance data.

Author Contributions: Conceptualization, D.X.; writing—original draft, X.Z. and D.X.; writing—review and editing, R.L., F.S.; formal analysis, X.Z. and F.S.; D.X.; data curation, D.X. and R.L. All authors have read and agreed to the published version of the manuscript.

Funding: This research was funded by the Second Tibetan Plateau Scientific Expedition and Research (STEP) program (2019QZKK0105), the Chinese National Natural Science Foundation of China (G42192553), Program of Shanghai Academic/Technology Research Leader (21XD1404500), the Shanghai Typhoon Research Foundation (TFJJ202107), the Chinese National Natural Science Foundation of China (G41805016), the research project of Heavy Rain and Drought-Flood Disasters in Plateau and Basin Key Laboratory of Sichuan Province in China (SZKT201904), the research project of the Institute of Atmospheric Environment, China Meteorological Administration, Shenyang in China (2020SYIAE02).

Data Availability Statement: The assimilated observations of AGRI L1 Full Disk, AGRI L1 GEO, and Cloud Mask L2 Full Disk were obtained freely from http://satellite.nsmc.org.cn. The ECMWF reanalysis data can be downloaded from http://rda.ucar.edu/datasets/ds113.0/ (accessed on 1 August 2022). Part of the software was associated with the National Center for Atmospheric Research (NCAR) using the new version 4.3 of the WRF and WRFDA system. The best-track data for Typhoon In-Fa are supported by the China Meteorological Administration (CMA). The reanalysis is provided by the 0.25° × 0.25° GFS from NCEP Global Forecast System, available at https://rda.ucar.edu/datasets/ds084.1/ (accessed on 1 August 2022). Figures were made with NCL version 6.6.2 from https://ncl.ucar.edu and Python version 3.3.8 from https://www.python.org.

Acknowledgments: We acknowledge the High Performance Computing Center of Nanjing University of Information Science & Technology for their support of this work.

Conflicts of Interest: The authors declare no conflict of interest.

References

1. Deber, J.C.; Wu, W.-S. The use of TOVS cloud-cleared radiances in the NCEP SSI analysis system. *Mon. Wea. Rev.* **1998**, *126*, 2287–2299. [CrossRef]
2. Poli, P. Assimilation of satellite observations of the atmosphere. *Comptes Rendus Geosci.* **2010**, *342*, 357–369. [CrossRef]
3. Zhang, P.; Lu, Q.F.; Hu, X.Q.; Gu, S.Y.; Yang, L.; Min, M.; Chen, L.; Xu, N.; Sun, L.; Bai, W.G.; et al. Latest Progress of the Chinese Meteorological Satellite Program and Core Data Processing Technologies *Adv. Atmos. Sci.* **2019**, *36*, 1027–1045. [CrossRef]
4. Bormann, N.; Duncan, D.; English, S.; Healy, S.; Lonitz, K.; Chen, K.; Lawrence, H.; Lu, Q.F. Growing operational use of FY-3 data in the ECMWF system. *Adv. Atmos. Sci.* **2021**, *38*, 1285–1298. [CrossRef]
5. Carminati, F.B.; Migliorini, S. All-sky Data Assimilation of MWTS-2 and MWHS-2 in the Met Office Global NWP System. *Adv. Atmos. Sci.* **2021**, *38*, 1682–1694. [CrossRef]
6. Liu, Z.Q.; Schwartz, C.S.; Snyder, C.; Ha, S.Y. Impact of assimilating AMSU-A radiances on forecasts of 2008 Atlantic tropical cyclones initialized with a limited-area ensemble Kalman filter. *Mon. Wea. Rev.* **2012**, *140*, 4017–4034. [CrossRef]
7. Schmit, T.J.; Li, J.; Ackerman, S.A.; Gurka, J.J. High-spectral- and high-temporal-resolution infrared measurements from geostationary orbit. *J. Atmos. Ocean. Technol.* **2009**, *26*, 2273–2292. [CrossRef]
8. Schmit, T.J.; Gunshor, M.M.; Menzel, W.P.; Gurka, J.J.; Li, J.; Bachmeier, A.S. Introducing the next-generation Advanced Baseline Imager on GOES-R. *Bull. Am. Meteorol. Soc.* **2005**, *86*, 1079–1096. [CrossRef]
9. Yang, C.; Liu, Z.Q.; Gao, F.; Childs, P.P.; Min, J.Z. Impact of assimilating GOES imager clear-sky radiance with a rapid refresh assimilation system for convection-permitting forecast over Mexico. *J. Geophys. Res. Atmos.* **2017**, *122*, 5472–5490. [CrossRef]
10. Zou, X.L.; Qin, Z.K.; Weng, F.Z. Improved coastal precipitation forecasts with direct assimilation of GOES-11/12 imager radiances. *Mon. Wea. Rev.* **2011**, *39*, 3711–3729. [CrossRef]
11. Zou, X.L.; Qin, Z.K.; Zheng, Y. Improved tropical storm forecasts with GOES-13/15 imager radiance assimilation and asymmetric vortex initialization in HWRF. *Mon. Wea. Rev.* **2015**, *143*, 2485–2505. [CrossRef]
12. Qin, Z.K.; Zou, X.L. Direct Assimilation of ABI Infrared Radiances in NWP Models. *IEEE J. Sel. Top. Appl. Earth Obs. Remote Sens.* **2018**, *11*, 2022–2033. [CrossRef]
13. Bessho, K.; Date, K.; Hayashi, M.; Ikeda, A.; Imai, T.; Inoue, H.; Kumagai, Y.; Miyakawa, T.; Murata, H.; Ohno, T.; et al. An Introduction to Himawari-8/9—Japan's New-Generation Geostationary Meteorological Satellites. *J. Meteorol. Soc. Jpn.* **2016**, *94*, 151–183. [CrossRef]
14. Zou, X.L.; Weng, F.Z.; Qin, Z.K.; Symposium, R.S. Direct assimilation of AHI and ABI infrared radiances in NWP models. *IEEE Trans. Geosci. Remote Sens.* **2017**, 290–292.
15. Sawada, Y.; Okamoto, K.; Kunii, M.; Miyoshi, T. Assimilating every-10-min himawari-8 infrared radiances to improve convective predictability. *J. Geophys. Res. Atmos.* **2019**, *124*, 2546–2561. [CrossRef]
16. Xu, D.M.; Liu, Z.Q.; Fan, S.Y.; Chen, M.; Shen, F.F. Assimilating all-sky infrared radiances from Himawari-8 using the 3DVar method for the prediction of a severe storm over North China. *Adv. Atmos. Sci.* **2021**, *38*, 661–676. [CrossRef]
17. Thibaut, M.; Florence, R.; Claude, F. Relative impact of polar-orbiting and geostationary satellite radiances in the Aladin/France numerical prediction system. *Quart. J. Roy. Meteor. Soc.* **2007**, *133*, 655–671.
18. Hutt, A.; Schraff, C.; Anlauf, H.; Bach, L.; Baldauf, M.; Bauernschubert, E.; Cress, A.; Faulwetter, R.; Fundel, F.; Köpken-Watts, C.; et al. Assimilation of SEVIRI Water Vapor Channels with an Ensemble Kalman Filter on the Convective Scale. *Front. Earth Sci.* **2020**, *8*, 2296–6463. [CrossRef]
19. Otkin, J.A.; Potthast, R. Assimilation of All-Sky SEVIRI Infrared Brightness Temperatures in a Regional-Scale Ensemble Data Assimilation System. *Mon. Wea. Rev.* **2019**, *147*, 4481–4509. [CrossRef]
20. Stengel, M.; Undén, P.; Lindskog, M.; Dahlgren, P.; Gustafsson, N.; Bennartz, R. Assimilation of SEVIRI infrared radiance with HIRLAM 4D-Var. *Quart. J. Roy. Meteor. Soc.* **2009**, *135*, 2100–2109. [CrossRef]
21. Wang, P.; Li, J.; Li, L.Z.; Lim, A.N.H.; Li, J.L.; Schmit, T.J.; Goldberg, M.D. The Impact of Cross-track Infrared Sounder (CrIS) Cloud-Cleared Radiances on Hurricane Joaquin (2015) and Matthew (2016) Forecasts. *J. Geophys. Res. Atmos.* **2017**, *122*, 13201–13218. [CrossRef]
22. Honda, T.; Miyoshi, T.; Lien, G.; Nishizawa, S.; Yoshida, R.; Adachi, S.A.; Terasaki, K.; Okamoto, K.; Tomita, H.; Bessho, K. Assimilating all-sky Himawari-8 satellite infrared radiances: A case of Typhoon Soudelor (2015). *Mon. Wea. Rev.* **2018**, *146*, 213–229. [CrossRef]
23. Honda, T.; Takino, S.; Miyoshi, T. Improving a precipitation forecast by assimilating all-sky himawari-8 satellite radiances: A case of Typhoon Malakas (2016). *J. Meteorol. Soc. Jpn.* **2019**, *15*, 7–11. [CrossRef]
24. Wang, Y.B.; He, J.Y.; Chen, Y.D.; Min, J.Z. The Potential Impact of Assimilating Synthetic Microwave Radiances Onboard a Future Geostationary Satellite on the Prediction of Typhoon Lekima Using the WRF Model. *Remote Sens.* **2021**, *13*, 886. [CrossRef]
25. Yang, J.; Zhang, Z.Q.; Wei, C.Y.; Lu, F.; Guo, Q. Introducing the New Generation of Chinese Geostationary Weather Satellites, Fengyun-4. *Bull. Am. Meteorol. Soc.* **2017**, *98*, 1637–1658. [CrossRef]
26. Chen, Y.D.; Shen, J.; Fan, S.Y.; Meng, D.M.; Wang, C. Characteristics of Fengyun-4A Satellite Atmospheric Motion Vectors and Their Impacts on Data Assimilation. *Adv. Atmos. Sci.* **2020**, *37*, 1222–1238. [CrossRef]
27. Zhang, W.J.; Hui, W.; Lyu, W.T.; Cao, D.J.; Li, P.F.; Zheng, D.; Fang, X.; Zhang, Y.J. FY-4A LMI observed lightning activity in Super Typhoon Mangkhut (2018) in comparison with WWLLN data. *J. Meteorol. Res.* **2020**, *34*, 336–352. [CrossRef]

28. Yin, R.Y.; Han, W.; Gao, Z.Q.; Li, J. Impact of High Temporal Resolution FY-4A Geostationary Interferometric Infrared Sounder (GIIRS) Radiance Measurements on Typhoon Forecasts: Maria (2018) Case with GRAPES Global 4D-Var Assimilation System. *Geophys. Res. Lett.* **2021**, *48*, e2021GL093672. [CrossRef]
29. Geng, X.W.; Min, J.Z.; Yang, C.; Wang, Y.B.; Xu, D.M. Analysis of FY-4A AGRI Radiance Data Bias Characteristics and a Correction Experiment. *Chin. J. Atmos. Sci.* **2020**, *44*, 679–694.
30. Zhu, J.; Shu, J.; Guo, W. Biases Characteristics Assessment of the Advanced Geosynchronous Radiation Imager (AGRI) Measurement on Board Fengyun-4A Geostationary Satellite. *Remote Sens.* **2020**, *12*, 2871. [CrossRef]
31. Lan, X.; Cheng, W.; Deng, Z.; Liu, J.J.; Wang, B.; Lu, B.; Wang, S.D.; Dong, L. Assimilation of the FY-4A AGRI Clear-Sky Radiance Data in a Regional Numerical Model and Its Impact on the Forecast of the "21·7" Henan Extremely Persistent Heavy Rainfall. *Adv. Atmos. Sci.* **2022**, 1–17. [CrossRef]
32. Bauer, P.; Auligné, T.; Bell, W.; Geer, A.; Guidard, V.; Heilliette, S.; Kazumori, M.; Kim, M.-J.; Liu, E.; McNally, A.; et al. Satellite cloud and precipitation assimilation at operational NWP centres. *Quart. J. Roy. Meteor. Soc.* **2011**, *137*, 1934–1951. [CrossRef]
33. Karlsson, K.-G.; Johansson, E.; Devasthale, A. Advancing the uncertainty characterisation of cloud masking in passive satelite imagery: Probabilistic formulations for NOAA AVHRR data. *Remote Sens. Environ.* **2015**, *158*, 126–139. [CrossRef]
34. Platnick, S.; King, M.D.; Ackerman, S.A.; Menzel, W.P.; Baum, B.A.; Riédi, J.C.; Frey, R.A. The MODIS cloud products: Algorithms and examples from Terra. *IEEE Trans. Geosci. Remote Sens.* **2003**, *41*, 459–473. [CrossRef]
35. English, S.J.; Eyre, J.R.; Smith, J.A. A cloud-detection scheme for use with satellite sounding radiances in the context of data assimilation for numerical weather prediction. *Quart. J. Roy. Meteor. Soc.* **1999**, *125*, 2359–2378. [CrossRef]
36. McNally, A.P.; Watts, P.D. A cloud detection algorithm for high-spectral-resolution infrared sounders. *Quart. J. Roy. Meteor. Soc.* **2003**, *129*, 3411–3423. [CrossRef]
37. Auligné, T. Multivariate minimum residual method for cloud retrieval. Part I: Theoretical aspects and simulated observation experiments. *Mon. Wea. Rev.* **2014**, *142*, 4383–4398. [CrossRef]
38. Auligné, T. Multivariate minimum residual method for cloud retrieval. Part II: Real observations experiments. *Mon. Wea. Rev.* **2014**, *142*, 4399–4415. [CrossRef]
39. Xu, D.M.; Auligne, T.; Descombes, G.; Snyder, C. A method for retrieving clouds with satellite infrared radiances using the particle filter. *Geosci. Model. Dev.* **2016**, *9*, 3919–3932. [CrossRef]
40. Dong, Y.H. FY-4 meteorological satellite and its application prospect. *J. Aerosp. Shanghai* **2016**, *33*, 1–8. (In Chinese)
41. Geer, A.J.; Bauer, P. Observation errors in all-sky data assimilation. *Quart. J. Roy. Meteor. Soc.* **2011**, *137*, 2024–2037. [CrossRef]
42. Barker, D.; Huang, X.Y.; Liu, Z.Q.; Auligné, T.; Zhang, X.; Rugg, S.; Ajjaji, R.; Bourgeois, A.; Bray, J.; Chen, Y.S.; et al. The Weather Research and Forecasting Model's Community Variational/Ensemble Data Assimilation System: WRFDA. *Bull. Am. Meteorol. Soc.* **2012**, *93*, 831–843. [CrossRef]
43. Saunders, R.; Hocking, J.; Turner, E.; Rayer, P.; Rundle, D.; Brunel, P.; Vidot, J.; Roquet, P.; Matricardi, M.; Lupu, C.; et al. An update on the RTTOV fast radiative transfer model (currently at version 12). *Geosci. Model Dev.* **2018**, *11*, 2717–2737. [CrossRef]
44. Wang, X.; Min, M.; Wang, F.; Guo, J.; Li, B.; Tang, S. Inter comparisons of Cloud Mask Products Among Fengyun-4A, Himawari-8, and MODIS. *IEEE Trans. Geosci. Remote Sens.* **2019**, *57*, 8827–8839. [CrossRef]
45. Barker, D.M.; Huang, W.; Guo, Y.R.; Bourgeois, A.J.; Xiao, Q.N. A Three-Dimensional Variational Data Assimilation System for MM5: Implementation and Initial Results. *Mon. Wea. Rev.* **2004**, *132*, 897–914. [CrossRef]
46. Parrish, D.F.; Derber, J.C. The national meteorological center's spectral statistical-interpolation analysis system. *Mon. Wea. Rev.* **1992**, *120*, 1747–1763. [CrossRef]
47. Hong, S.-Y.; Dudhia, J.; Chen, S.-H. A revised approach to ice microphysical processes for the bulk parameterization of clouds and precipitation. *Mon. Wea. Rev.* **2004**, *132*, 103–120. [CrossRef]
48. Iacono, M.J.; Delamere, J.S.; Mlawer, E.J.; Shephard, M.W.; Clough, S.A.; Collins, W.D. Radiative forcing by long-lived greenhouse gases: Calculations with the AER radiative transfer models. *J. Geophys. Res.* **2008**, *113*, D13103. [CrossRef]
49. Hong, S.-Y.; Noh, Y.; Dudhia, J. A new vertical diffusion package with an explicit treatment of entrainment processes. *Mon. Wea. Rev.* **2006**, *134*, 2318–2341. [CrossRef]
50. Chen, F.; Dudhia, J. Coupling an advanced land-surface/hydrology model with the Penn State/NCAR MM5 modeling system. Part I: Model description and implementation. *Mon. Wea. Rev.* **2001**, *129*, 569–585. [CrossRef]
51. Tewari, M.; Chen, F.; Wang, W.; Dudhia, J.; LeMone, M.A.; Mitchell, K.; Ek, M.; Gayno, G.; Wegiel, J.; Cuenca, R. Implementation and verification of the unified NOAH land surface model in the WRF model. In Proceedings of the 20th Conference on Weather Analysis and Forecasting/16th Conference on Numerical Weather Prediction, Seattle, WA, USA, 13 May–25 June 2004; pp. 11–15.
52. Dee, D.P.; Uppala, S.M.; Simmons, A.J.; Berrisford, P.; Poli, P.; Kobayashi, S.; Andrae, U.; Balmaseda, M.A.; Balsamo, G.; Bauer, P.; et al. The ERA-Interim reanalysis: Configuration and performance of the data assimilation system. *Quart. J. Roy. Meteor. Soc.* **2011**, *137*, 553–597. [CrossRef]